

Automated detection of delamination and disbond from wavefield images obtained using a scanning laser vibrometer

This article has been downloaded from IOPscience. Please scroll down to see the full text article.

2011 Smart Mater. Struct. 20 045017

(<http://iopscience.iop.org/0964-1726/20/4/045017>)

View [the table of contents for this issue](#), or go to the [journal homepage](#) for more

Download details:

IP Address: 143.248.122.175

The article was downloaded on 30/03/2011 at 15:22

Please note that [terms and conditions apply](#).

Automated detection of delamination and disbond from wavefield images obtained using a scanning laser vibrometer

H Sohn¹, D Dutta^{2,5}, J Y Yang¹, M DeSimio³, S Olson³ and E Swenson⁴

¹ Department of Civil and Environmental Engineering, Korea Advanced Institute of Science and Technology, Daejeon 305701, Korea

² Department of Civil and Environmental Engineering, Carnegie Mellon University, Pittsburgh, PA 15213, USA

³ University of Dayton Research Institute, Dayton, OH 45469, USA

⁴ Air Force Institute of Technology, Wright-Patterson AFB, OH 45430, USA

E-mail: debaditya.dutta@gmail.com

Received 29 November 2010, in final form 16 February 2011

Published 23 March 2011

Online at stacks.iop.org/SMS/20/045017

Abstract

The paper presents signal and image processing algorithms to automatically detect delamination and disbond in composite plates from wavefield images obtained using a scanning laser Doppler vibrometer (LDV). Lamb waves are excited by a lead zirconate titanate transducer (PZT) mounted on the surface of a composite plate, and the out-of-plane velocity field is measured using an LDV. From the scanned time signals, wavefield images are constructed and processed to study the interaction of Lamb waves with hidden delaminations and disbonds. In particular, the frequency–wavenumber ($f-k$) domain filter and the Laplacian image filter are used to enhance the visibility of defects in the scanned images. Thereafter, a statistical cluster detection algorithm is used to identify the defect location and distinguish damaged specimens from undamaged ones.

(Some figures in this article are in colour only in the electronic version)

1. Introduction

In recent years, there has been an increasing demand for structural health monitoring (SHM) that appraises users of the integrity and safety of the structure being monitored [1, 2]. SHM often infers the current condition of the structure based on a stream of data collected from installed sensors. Guided ultrasonic waves have emerged as one of the most prominent tools for SHM due to their well-established theories, ability to detect small damage within relatively large inspection areas, and recent advancements in transducer technologies used for guided wave sensing and excitation.

Guided waves are specific types of elastic waves confined by the boundaries of a structure. For instance, when an isotropic plate structure is excited at a high frequency,

the top and bottom surfaces of the plate ‘guide’ the elastic waves to propagate in the directions of the plate, producing a specific type of guided waves called Lamb waves [3–5]. Various types of transducers can be used to excite and sense guided waves. The most commonly used transducers include angled piezoelectric wedge transducers, comb transducers, electromagnetic acoustic transducers and surface-bonded piezoelectric wafer transducers [6–10]. Some transducers, such as polyvinylidene fluoride (PVDF) and fiber optic sensors [11, 12], are mainly used for sensing applications. Although each transducer mentioned above has its own set of strengths and weaknesses, all are primarily used for discrete point measurements. Therefore, a dense array of transducers is required to achieve a good spatial resolution and cover a large inspection area. Moreover, the embedding of sensors and the associated instrumentation can be a source of additional mass and may disturb elastic waves.

⁵ Author to whom any correspondence should be addressed.

A potential solution to this problem is to use non-contact scanning laser techniques to create wavefield images with a high spatial resolution [13]. One such technique is to excite a fixed point using a conventional piezoelectric transducer and scan the guided wave response across the surface of the structure using an LDV [14–16]. Previous works in this field include the detection of fatigue cracks from the variation of the ultrasonic amplitude profile [14, 15] and the use of f – k domain filtering to locate scatterers in the ultrasonic medium, some of which could be defects [16]. Another technique is to use a pulsed laser source to generate guided waves at arbitrary locations, then corresponding responses are measured at a single point using a conventional ultrasonic transducer. The wavefield images are then constructed using the principle of dynamic reciprocity [17–19]. Note that the wavefield imaging discussed above is different from the traditional phased array ultrasonic imaging techniques in which time-of-flight or wave attenuation information is used to image all reflectors in the ultrasonic medium [20, 21]. Alternatively, fully non-contact ultrasonic C-scans may be performed using laser based ultrasound generation as well as sensing [22].

In a recent study, unique wave patterns were observed to arise when ultrasonic waves interact with delamination, and signal and image processing techniques were proposed to extract such unique patterns from the original wavefield, thereby highlighting the damage location in the scan image [23]. In this paper, image processing algorithms are proposed to automatically detect the presence of damage from the scan images without requiring human intervention and extend the concept to disbond detection.

This paper is organized in two main sections. Section 2 describes the signal and image processing techniques to automatically detect delamination from the original scanned wavefield data. The techniques are experimentally verified on a composite plate specimen with an impact-induced delamination. Section 3 provides parallel experimental results for a composite plate with a blade induced disbond. The paper concludes with a brief summary and critique in section 4.

2. Delamination detection in a multi-layer composite plate

In this section, experimental wavefield images from a composite plate with an internal delamination are obtained using an LDV. Standing waves are formed when ultrasonic waves interact with the delamination, and signal and image processing techniques are proposed to highlight such interactions. Thereafter, a statistical image processing technique is developed to distinguish between images obtained from damaged specimens and those obtained from undamaged ones.

2.1. Experimental setup

The composite plate tested in this study is shown in figure 1. The 27.5 cm × 27.5 cm × 1.8 mm plate is composed of IM7 graphite fibers with 977-3 resin material, and consists of 12 plies with a layup of $[0/\pm 45/0/\pm 45]_s$. The test article

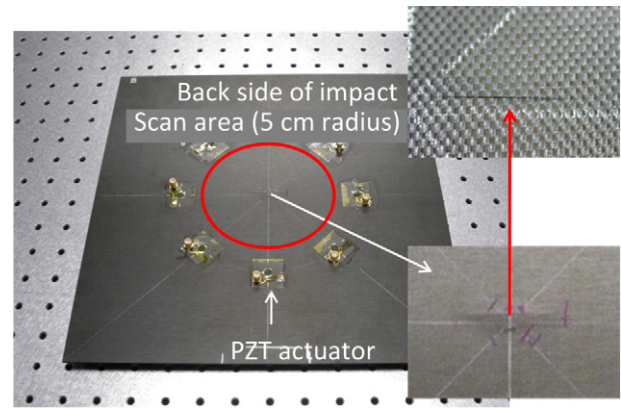


Figure 1. A multi-layer composite plate with impact-induced delamination.

was subjected to impact, and the formation of an internal delamination near the center of the plate was confirmed from independent nondestructive thermographic imaging, as shown in figure 2. The 3 cm long damage area could be seen on the back side of the plate shown in figure 1, but only a small dent, barely visible to the naked eye, was visible on the front (impacted) side.

Figure 3 shows the overall configuration of the experimental setup. A piezoelectric wafer transducer (6.35 mm diameter × 0.254 mm thick, PZT-5A material) was powered by an arbitrary waveform generator (AWG), and a signal amplifier was used to generate guided waves in the test article. The guided wave responses within the specified area were sensed by the LDV, and the data were collected by a built-in data acquisition system. The data were then exported to the MATLAB® software program and processed on a personal computer.

A 5.5 cycle tone burst signal with 100 kHz center frequency was used as the input waveform. The output voltage from the AWG was ± 10 V and was amplified to ± 50 V using a power amplifier before being applied to the actuator. One of the eight piezoelectric transducers was designated as the actuator (figure 1).

The guided waves were measured by a Polytec PSV-400-M4 scanning LDV. The 1D vibrometer used in this study measures the out-of-plane velocity of a target point using the principle of the Doppler frequency-shift effect on light waves [24]. For the 100 kHz excitation used in this study, only the fundamental symmetric and anti-symmetric modes are excited. The dispersion curves up to 150 kHz calculated using the bulk material properties along two principal orthogonal directions of the composite plate are shown in figure 4. Furthermore, the out-of-plane velocity component of the anti-symmetric mode is more strongly excited than that of the fundamental symmetric component. Therefore, the 1D laser vibrometer predominantly measures the anti-symmetric mode [25]. The wavelength corresponding to the fundamental anti-symmetric Lamb mode was found to be about 1.2 cm.

The laser vibrometer was placed about 0.9 m away from the test article, and the sensitivity of the velocity measurement was set to $10 \text{ mm s}^{-1} \text{ V}^{-1}$. The spatial grid density was

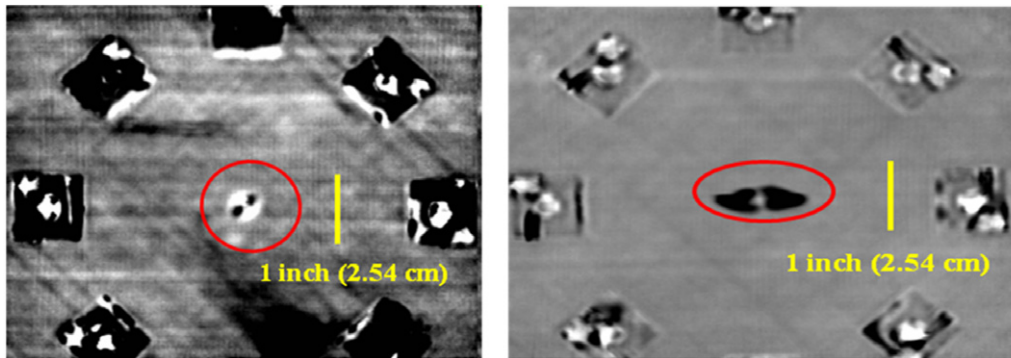


Figure 2. Thermographic images of the composite plate: impact surface (left) and back surface (right).

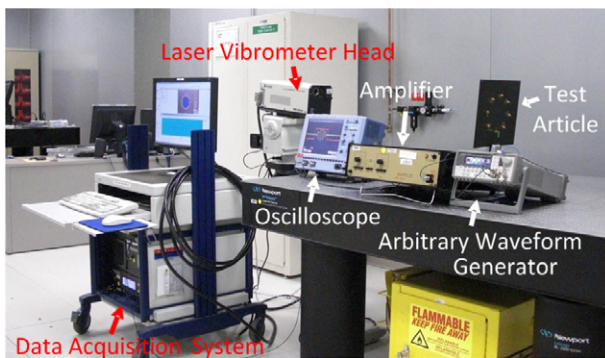


Figure 3. Overall configuration for the laser based guided wave excitation and sensing experiment.

9 points per centimeter and the temporal sampling rate was 2.56 MHz. The time response at each measurement point was averaged 20 times to improve the signal-to-noise ratio, and a 75–125 kHz band pass filter was applied to reduce noise outside the driving frequency band. Approximately 40 min were required to scan a circular area with 5 cm radius containing about 6400 scan points (figure 1).

2.2. Standing waves produced by delamination

The data are stored in a universal file format and exported to the MATLAB® software program. The raw data contain time signals from each of the scanned points. Using MATLAB® graphic tools, a wave propagation video is created where each frame in the video represents the out-of-plane velocity field

across the scanned surface of the target specimen at a particular instant in time. Snapshots at three representative time instants are shown in figure 5. All images are plotted in RGB scale where low to high values are mapped from blue to red with green indicating middle range values. The location of the delamination is marked with a box in figure 5. In figure 5(a), the incident waves can be clearly seen, and the interaction with the delaminated area is apparent in figure 5(b). Ultrasonic oscillations at the delamination location can be observed long after the incident waves had passed the delaminated area (figure 5(c)). A similar phenomenon was observed by Krohn *et al* [26] and Willemann *et al* [27], and a possible explanation for this phenomenon is given below.

Figure 6 shows a schematic through-the-thickness side view of a delamination. The incident waves enter the delamination zone, split, and then propagate independently through the upper and lower laminates. A significant portion of these waves is reflected back from the exit. The reflected waves travel through the laminates and undergo reflection again at the original entrance. Numerical simulations by Hayashi and Kawashima using the strip element method have confirmed such multiple reflections taking place inside the delaminated zone [28, 29]. As a consequence of multiple reflections at the entrance and the exit of the delaminated area, a considerable amount of ultrasonic energy is trapped inside the individual laminates.

Now, the ultrasonic waves reflected from opposite ends of the delamination travel in opposite directions and interfere to produce standing waves according to the following equation:

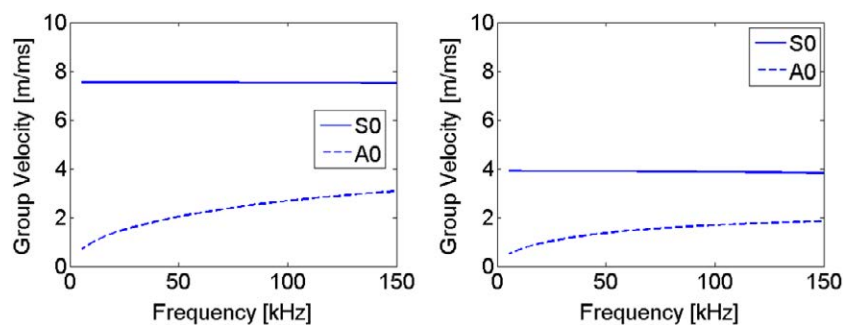


Figure 4. Dispersion curves along two principal orthogonal directions of the composite plate.

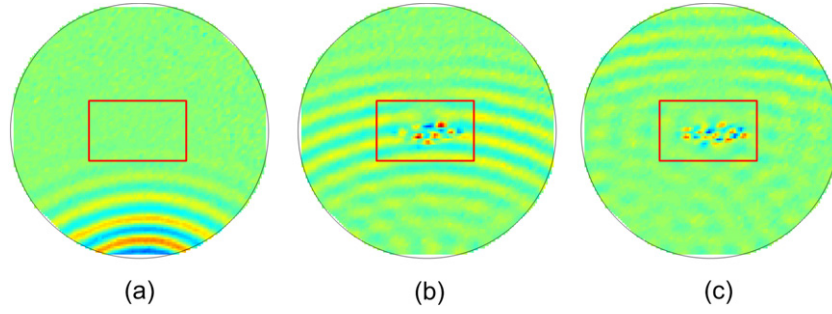


Figure 5. Laser vibrometer imaging of Lamb wave propagation in a 1.8 mm thick graphite plate containing delamination. Standing waves are observed at the delamination site. (a) 99 μ s, (b) 139 μ s and (c) 180 μ s.

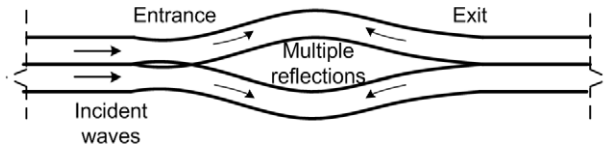


Figure 6. Schematic showing a through-the-thickness side view of a delamination with multiple reflections inside the delamination zone.

$$\begin{aligned}
 & A \cos(\omega t - kx) + B \cos(\omega t + kx + \phi) \\
 &= \underbrace{2B \cos(k\bar{x}) \cos\left(\omega t + \frac{\phi}{2}\right)}_{\text{Standing wave}} \\
 &+ (A - B) \cos\left(\omega t - k\bar{x} + \frac{\phi}{2}\right). \quad (1)
 \end{aligned}$$

In equation (1), A and B are the amplitudes of the waves propagating in opposite directions ($B < A$ without loss of generality); ω and k are the frequency and wavenumber of the propagating waves; ϕ is an arbitrary phase; t and x represent time and space coordinates, respectively; and \bar{x} is the zero-shifted coordinate given by $\bar{x} = x + \frac{\phi}{2k}$. The first term in the right-hand side of the equation represents the standing waves at delamination while the second one represents the part of the wave that propagates. The standing waves remain trapped inside the delamination site long after the incident waves have passed. With time, however, the standing waves subside as the ultrasonic energy leaks out through the boundaries of the delamination and attenuates. Equation (1) describes the propagation and interference of pure longitudinal waves or pure shear waves. Although the equations describing Lamb waves would be more complex, equation (1) captures the essence of standing wave formation.

2.3. Filtering techniques used to highlight delamination

Next, we propose a ‘standing wave filter’ which is essentially a signal processing technique to isolate only the standing wave components from a given wavefield. The first step is to convert the velocity field (v) from the space–time domain (x, y, t) to the f – k domain (k_x, k_y, ω) using a three-dimensional Fourier transform (3D FT) [16]:

$$\begin{aligned}
 V(k_x, k_y, \omega) &= \int_{-\infty}^{\infty} \int_{-\infty}^{\infty} \int_{-\infty}^{\infty} v(x, y, t) \\
 &\times e^{-i(k_x x + k_y y + \omega t)} dx dy dt. \quad (2)
 \end{aligned}$$

Here, $V(k_x, k_y, \omega)$ corresponds to the wavefront of frequency ω traveling in the vector direction $-k_x \hat{x} - k_y \hat{y}$, where \hat{x} and \hat{y} are the unit vectors along the x and y axes, respectively. A standing wave can be viewed as a superposition of two waves of equal amplitude propagating in opposite directions over the same spatial region at the same time instant. If the two waves traveling in opposite directions have different amplitudes, then the amplitude corresponding to the weaker wave will be the amplitude of the standing wave, as described in equation (1). Therefore, standing waves can be obtained from $V(k_x, k_y, \omega)$ as follows:

$$\begin{aligned}
 V_{sw}(k_x, k_y, \omega) &= V_{sw}(-k_x, -k_y, \omega) \\
 &= \min[|V(k_x, k_y, \omega)|, |V(-k_x, -k_y, \omega)|] \forall \omega \quad (3)
 \end{aligned}$$

where the subscript sw stands for standing waves. The processing steps described in this section are all implemented in MATLAB in the discrete-time paradigm. The range of ω in equation (3) is below the Nyquist frequency. The portion of V_{sw} above the Nyquist frequency is modified to force the conjugate symmetry condition. Upon filtering, the residual signal can be transformed back to the space–time domain using an inverse 3D FT:

$$\begin{aligned}
 v_{sw}(x, y, t) &= \frac{1}{2\pi} \int_{-\infty}^{\infty} \int_{-\infty}^{\infty} \int_{-\infty}^{\infty} V_{sw}(k_x, k_y, \omega) \\
 &\times e^{i(k_x x + k_y y + \omega t)} dk_x dk_y d\omega. \quad (4)
 \end{aligned}$$

This filtered wavefield $v_{sw}(x, y, t)$ contains only standing wave components that are present in the originally scanned wavefield. For example, if the process described above is applied to the wavefield in equation (1), the resulting field will only contain the standing wave component: $2B \cos(k\bar{x}) \cos(\omega t + \frac{\phi}{2})$. Figure 7 shows the time sequenced wavefields when the originally measured wavefield images in figure 5 are passed through the standing wave filter. The incident waves in figure 5(a) are filtered out in figure 7(a). In figure 7(b), standing waves can be observed at the delamination location. Although mitigated, standing waves are found to be present long after the incident waves have passed (figure 7(c)).

To visualize the total amount of standing wave energy experienced at location (x, y) at time t , a mass-normalized value of the cumulative kinetic energy (E_{sw}) is computed as follows:

$$E_{sw}(x, y, t) = \int_{\tau=0}^t \frac{1}{2} v_{sw}^2(x, y, \tau) d\tau. \quad (5)$$

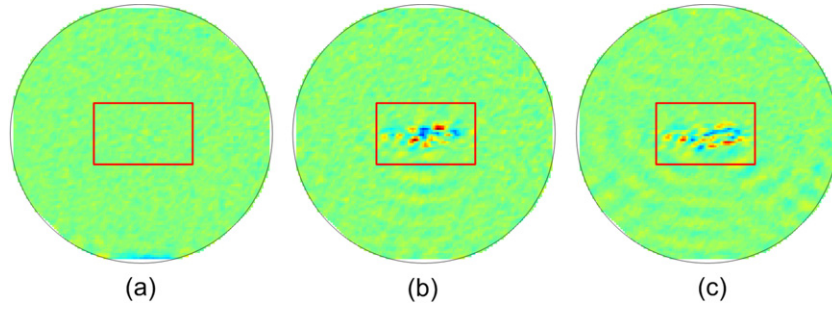


Figure 7. Isolating the standing wave components from the velocity fields in figure 5. (a) 99 μs , (b) 139 μs and (c) 180 μs .

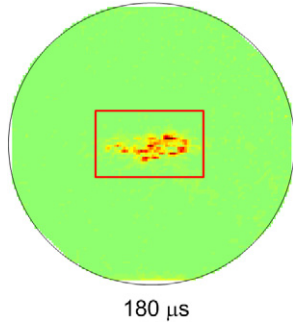


Figure 8. Accumulated mass-normalized kinetic energy corresponding to the standing wavefields in figure 7.

The cumulative energy field when plotted at the end of the scanning duration (180 μs) helps to locate and visualize the delamination (figure 8).

Another way to highlight the interaction of ultrasonic waves with delamination is by simply considering the total amount of ultrasonic energy that has passed through a certain point. As standing waves are formed, ultrasonic energy remains trapped inside the delamination region for a longer time as opposed to other locations where the incident or reflected waves are present only for a short time. Therefore, by computing the accumulated mass-normalized kinetic energy (E_c), it is possible to accentuate the delamination location in the entire scanned area (figure 9) [27]:

$$E_c(x, y, t) = \int_{\tau=0}^t \frac{1}{2} v^2(x, y, \tau) d\tau. \quad (6)$$

Of course, if the distance between the actuator PZT and the damage is relatively large, then E_c at the delamination would

be smaller compared to E_c in the near-field of the PZT. In this case, the attenuation of the ultrasonic wave would take precedence over standing wave formation. However, we do expect to see a sudden rise in E_c in the delaminated area compared to its immediate neighborhood. In contrast, the energy drop due to attenuation is less sudden. This effect is somewhat visible in figure 9. In the following paragraph we describe a method to extract this feature of sudden energy rise due to standing wave formation while suppressing the relatively smoother change in energy level due to attenuation.

The visual indication of the delamination can be enhanced even further by image processing. A well-known blob detection algorithm called Laplacian image filtering [30] is applied to the image in figure 9(c) to produce figure 10. A Laplacian filter is a discrete spatial second derivative operator that detects sudden intensity changes in an image. The level of discretization is the same as the grid spacing of the scanning laser vibrometer. The second derivative is computed from the convolution of a Laplacian mask with the original image. The Laplacian mask (\mathbf{L}) used in the filter is given by

$$\mathbf{L} = \begin{bmatrix} -1 & -1 & -1 \\ -1 & 8 & -1 \\ -1 & -1 & -1 \end{bmatrix}. \quad (7)$$

It can be observed from figure 9 that only the sudden intensity rise due to standing wave formation is captured by the Laplacian filter. The gradual variation of intensity due to attenuation is considerably suppressed.

Based on the theory proposed in section 2.2, the damage detection technique discussed in this paper is expected to be effective for delaminations only. A small cut or a crack running perpendicularly to the surface of a thin plate cannot produce

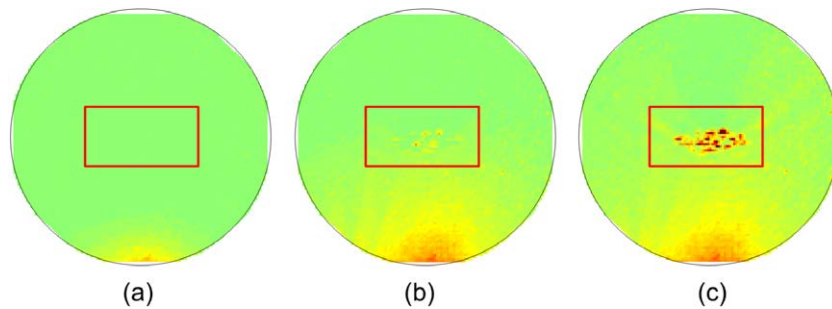


Figure 9. Accumulated mass-normalized kinetic energy corresponding to the velocity fields in figure 5. (a) 99 μs , (b) 139 μs and (c) 180 μs .

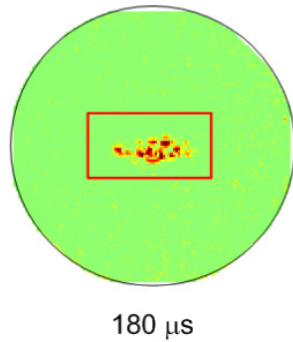


Figure 10. Effect of applying a Laplacian image filter to the image in figure 9(c).

standing waves. The basis of standing wave formation is that the defect boundary must enclose a sizable area within which the waves experiencing multiple reflections from the boundaries will interact. Unlike delaminations, a cut or a perpendicular crack does not enclose an area, and therefore standing waves are not formed in the presence of such defects.

It is postulated at this point that the area enclosed by the delamination boundary should be of comparable dimensions to the spatial length of the probing ultrasonic waveform. If the delaminated area is too large, the waves reflected from the defect boundaries will cross each other without forming a stable standing wave. If the area is too small, the waves would hit the boundaries too often and leak out of the damaged area too quickly to form a stable standing wave. A more detailed study of the effect of damage size on the damage detection algorithm (including the Laplacian filtering) is envisioned as part of future work.

2.4. Automated damage detection

The image processing techniques described so far make the defect region conspicuous in the background of the entire scan area, thereby making it easier for investigators to identify and locate the damage. However, manual monitoring of the infrastructure is time and labor intensive. Automated damage detection can significantly reduce the cost of infrastructure monitoring. In this subsection, we describe a procedure to automatically detect the defect location from the processed scan images. This automatic detection algorithm needs not only to detect the damage but also to correctly recognize undamaged objects.

The result from a representative undamaged composite plate specimen is shown in figure 11, after the original wave propagation image has been processed using the Laplacian filtering technique described earlier. It can be observed that high intensity values in the processed scan image (red dots) from the delaminated specimen (figure 10) are clustered together in the defect region while the high intensity values in the undamaged specimen scan (figure 11) appear scattered across the scan area, especially near the outer boundary of the scan area. The latter can be explained by the working principle of a laser Doppler vibrometer. In the case of one-dimensional laser vibrometers, which measure the out-of-plane velocity

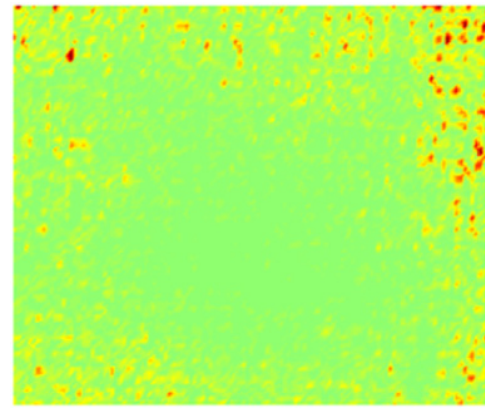


Figure 11. Scanned image from an undamaged composite plate after the application of the Laplacian image filtering technique. The actuator PZT is located near the bottom-left corner of the scanned area.

component, the signal-to-noise ratio of the measured ultrasonic signals drops as the laser incidence angle increases [24]. In our experiments, the laser head was placed directly over the center of the scan area, which resulted in slant incidence (nearly 5°) of the laser beam towards the edges and therefore caused a deterioration in the signal-to-noise ratio (SNR) at the edges. In figure 11, the actuator PZT was placed near the bottom-left corner of the scanned area. This explains the lower SNR and greater number of error points at the top, especially at the top right-hand side of the scanned area. Note that figure 11 shows the scanned image after Laplacian filtering, which is in effect a spatial second derivative operator. Therefore, the scattered high intensity dots in this image are interpreted as noise resulting in higher fluctuation in the field intensity rather than a higher value of the field intensity itself.

The automated damage detection algorithm is designed in two steps. In the first step, the high intensity values are identified using outlier analysis. In the second step, a cluster analysis is performed to check whether the outliers detected from the previous step are clustered or scattered. It is assumed that there is only one defect in the scanned area. This is a reasonable assumption considering that we might be able to detect damage at one location before damage at another location occurs.

The first step in the algorithm is to detect the high intensity outliers in the scan image. In this research, three sigma outlier detection [31] is utilized. Consider a unimodal distribution with mean μ and standard deviation σ . The probability that a random variable will assume a value more discordant than $(\mu \pm 3\sigma)$ is less than 5% [31]:

$$\Pr(|X - \mu| \geq 3\sigma) \leq \frac{4}{9} \times \frac{\sigma^2}{(3\sigma)^2} = 0.049. \quad (8)$$

This probability is even lower when we just consider values over $(\mu + 3\sigma)$. Since the intensity distributions in the processed images are found to be approximately unimodal (e.g. figure 12), equation (8) is used to detect the high intensity outliers. The outliers detected in the processed scan images from the undamaged and damaged specimens are shown in

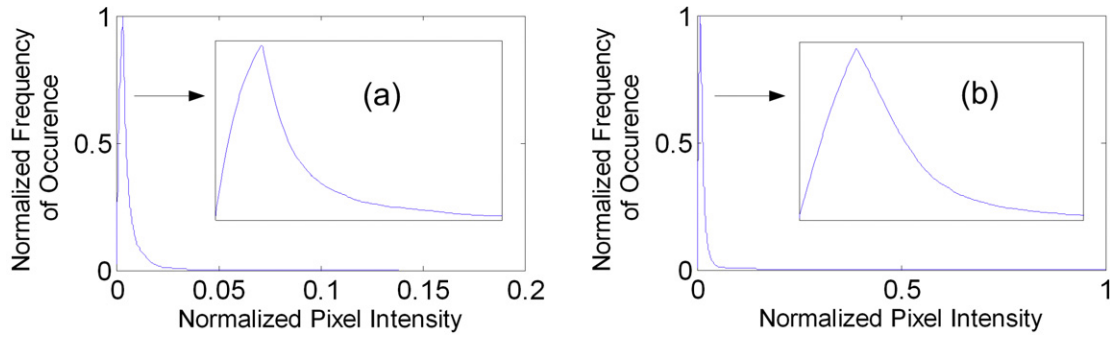


Figure 12. Distribution of the intensity values. (a) Undamaged (figure 11); (b) damaged (figure 10).

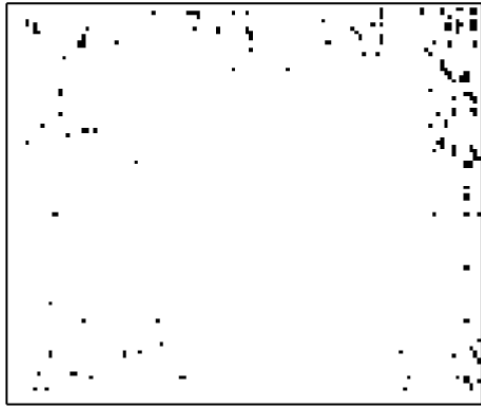


Figure 13. Outlier intensity values identified in the processed scan image (figure 11) from the undamaged composite plate.

figures 13 and 14 respectively. As expected, the outliers in the damaged specimen scan are clustered at the defect location while those in the undamaged specimen scan are scattered, especially near the boundary.

Once the outliers are identified, a cluster detection algorithm is used. The process is based on the complete spatial randomness (CSR) hypothesis, which assumes that if there is no apparent cluster in a spatial distribution of points, then the points are randomly distributed in space with Poisson distribution [32]. The Poisson parameter, λ , is given by

$$\lambda = \frac{n}{A} \quad (9)$$

where n is the number of outliers and A is the scan area. Under this hypothesis, one can argue that the area enclosing r outliers (A_r : $1 \leq r \leq n$) is gamma distributed with parameters a and b given by $a = r$, $b = \frac{1}{\lambda}$:

$$A_r \sim \text{gamma} \left(a = r, b = \frac{1}{\lambda} \right). \quad (10a)$$

The probability density function (pdf) of A_r is given by

$$f(A_r; a, b) = A_r^{a-1} \frac{e^{-A_r/b}}{\Gamma(a)b^a} \quad (10b)$$

where Γ is the symbol for the gamma function.

We thereby define the test statistic for cluster detection in the following manner. First, the coordinates of the centroid

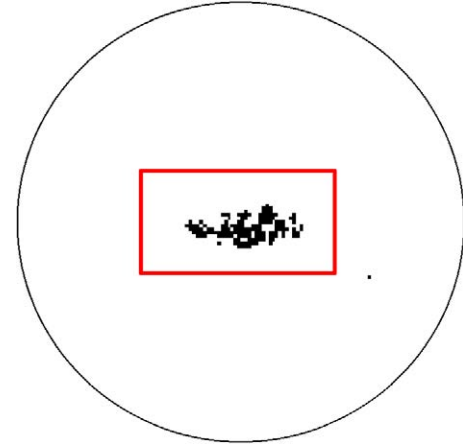


Figure 14. Outlier intensity values identified in the processed scan image (figure 10) from the composite plate with internal delamination.

of the outlier points are evaluated. Then, the distance from the centroid to each outlier point is computed and arranged in ascending order. Let this distance be d_r for the r th outlier point in the sorted distance array. Then, the probability, p_r , that the circle with radius d_r would contain r points without damage is

$$p_r = P \left[A_r = a_r | A_r \sim \text{gamma} \left(a = r, b = \frac{1}{\lambda} \right) \right] \quad (11)$$

where $a_r = \pi d_r^2$. This probability p_r is evaluated repeatedly for each outlier point $1 \leq r \leq n$, and a P -value is computed as the average of these n probability values:

$$P - \text{value} = \frac{1}{n} \sum_{r=1}^n p_r. \quad (12)$$

The P -value is the level of significance with which the outlier points are scattered randomly and are not clustered in space. Therefore, in our application, a lower P -value would indicate damage. Using the above procedure, the P -value for the delaminated composite specimen was found to be 0.04% while for the undamaged specimen the P -value was 65%. It is expected that a larger defect size will result in a smaller P -value because more outliers will be clustered in the defect area. While the P -value is not directly related to the distribution of the intensity values (as shown in figure 12 for example),

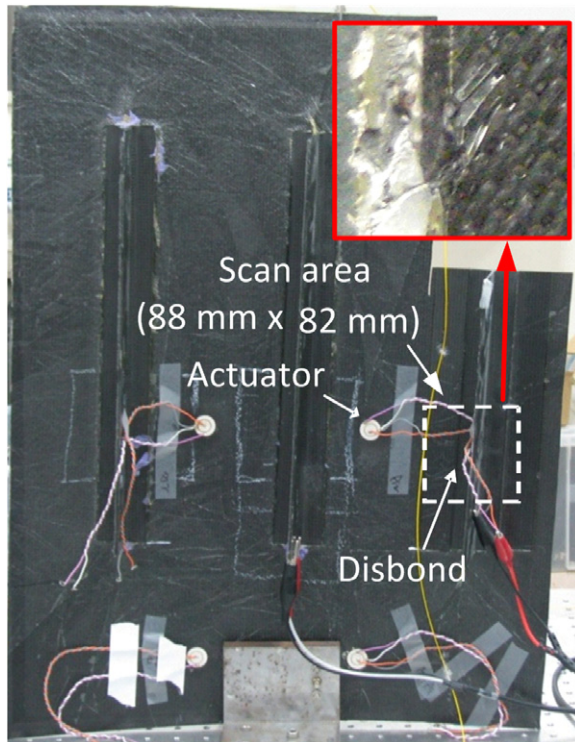


Figure 15. A composite wing fitted with spars. A blade induced disbond was introduced between the plate and one of the spars.

the distribution indirectly influences the P -value by affecting which intensity values would be classified as outliers. The threshold P -value (to distinguish damaged and undamaged specimens) for a particular application is to be chosen by the user depending on the desired level of confidence in the damage indicator.

As a closing note to this section, the cluster detection algorithm described in this study is not fit for detecting multiple clusters. Therefore, the presence of more than one defect in the scanned area might confuse the cluster detection algorithm and result in missing the presence of damage (false negative).

3. Disbond detection in a composite wing with multiple spars

In this section, wavefield images are presented from a composite wing specimen with a blade induced disbond

between the wing surface and one of the spars. Once again, the Laplacian image filtering technique described in section 2.3 was found to be effective in highlighting the damage location, and the statistical spatial image processing technique described in section 2.3 was used to identify the defect automatically.

The composite specimen tested for disbond is shown in figure 15. This 11.8 cm \times 15.7 cm \times 2 mm plate is fitted with three composite spars and has a 4 cm \times 6 cm area removed from the top right corner. The details of the fabrication materials were not provided to the authors. A blade induced disbond was introduced between the wing surface and the base of one of the spars, as shown in figure 15. The disbond is semicircular in shape and about 1.2 cm in diameter.

The input signal, data acquisition settings and vibrometer settings were identical to those in section 2.1. The scan was done on the external surface of the wing (i.e., on the opposite side to what is shown in figure 15). The scanned area was a 8.8 cm \times 8.2 cm rectangle containing about 6000 scan points. The longest disbond dimension was 2 cm and the wavelength of the fundamental anti-symmetric mode was about 1.5 cm.

Figure 16 shows snapshots of wave propagation in the structure at certain time instants. The location of the disbond is marked with a box in figure 16. As can be observed from figure 16(b), the out-of-plane velocity of the ultrasonic wave is comparatively high at the disbond location. This is more evident from the accumulated kinetic energy images in figure 17. Unlike delamination, a disbond is not bounded on all sides, and a substantial part of the waves reflected from the edge of the disbond escapes through the open end of the disbond (figure 18). Therefore the standing waves which are formed in a delamination do not occur in the case of a disbond. Notice that, unlike figure 5(c), standing waves are not observed in the disbond area in figure 16(c). However, convergent waves reflected from a roughly semicircular disbond edge (as is the case here) remain inside the disbond region at least momentarily and interfere with the incident waves (figure 18). This interference causes high amplitude oscillation inside the disbond region and provides an explanation for the higher accumulated energy observed at the disbond location in figure 17. The effect of such interference, however, is not as pronounced as it was in the case of standing wave production due to delamination (section 2). In fact, one can see from figure 16 that the level of accumulated energy in the disbond area is hardly greater than that caused by ordinary interaction of the incident waves with those reflected from the spar.

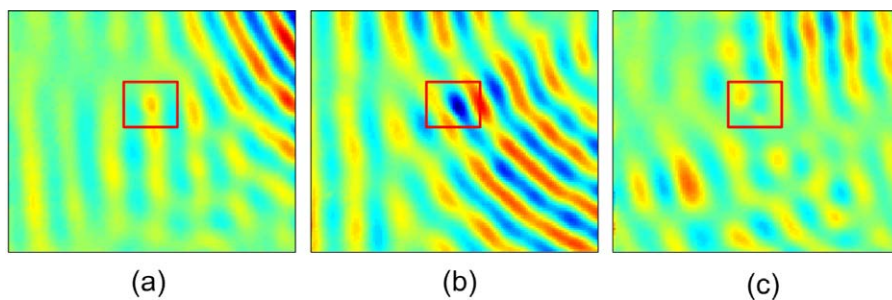


Figure 16. Snapshots of Lamb wave propagation on the wing surface. (a) 107 μ s, (b) 141 μ s and (c) 170 μ s.

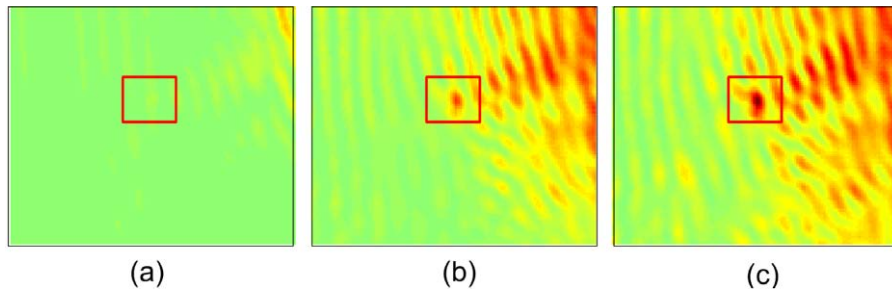


Figure 17. Accumulated mass-normalized kinetic energy corresponding to the wavefield in figure 16. (a) 107 μ s, (b) 141 μ s and (c) 170 μ s.

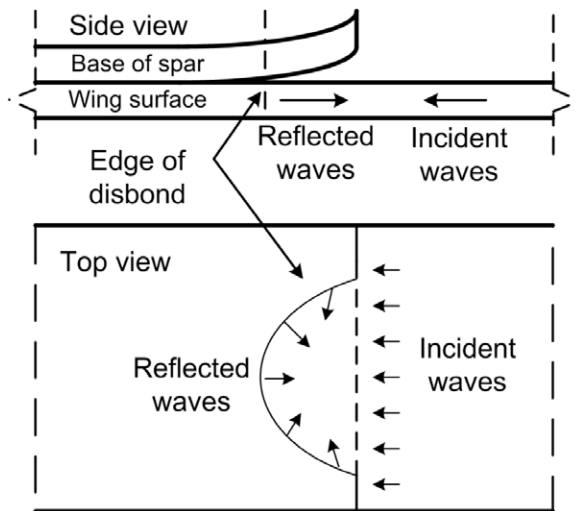


Figure 18. Schematic showing the interaction of ultrasonic waves with a disbond.

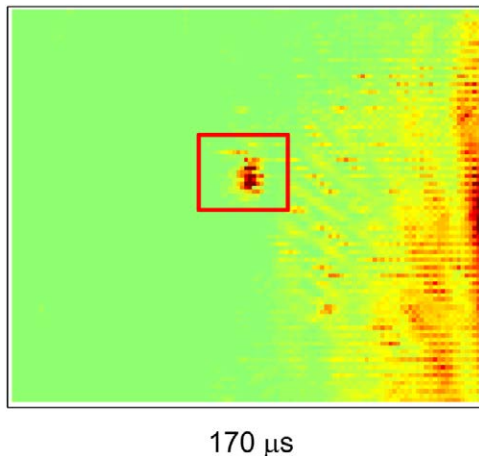


Figure 19. Application of a Laplacian image filter to highlight the disbond location.

Still, the Laplacian image filter was found to be effective in highlighting the sudden intensity rise at the disbond location (figure 19), although the performance of the filter was not as dramatic as it was in the case of the delamination (section 2.3). As a note, the application of a standing wave filter does not help in the case of disbond detection (which is expected).

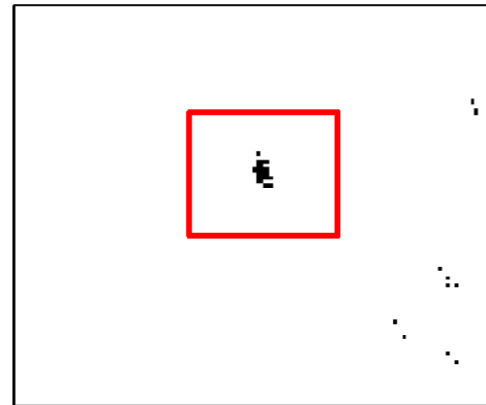


Figure 20. Outlier intensity values identified in the processed scan image (figure 19) from the composite wing with a blade induced disbond.

The statistical image processing technique described in section 2.3 resulted in a P -value of 10%. A few outliers are found outside the defect area where the ordinary interaction between incident and reflected waves produced speckled patterns with energy levels comparable to that in the disbond area (figure 20). These outliers away from the defect location pull the centroid towards them and confuse the algorithm to some extent, resulting in a relatively higher P -value.

4. Conclusions

This paper studied the applicability of non-contact wavefield imaging techniques to detect delamination and disbond in composite structures. A piezoelectric transducer was used to excite guided ultrasonic waves in the target structure and a laser vibrometer was used to image the resulting ultrasonic velocity field. The wavefield images thus obtained were further processed to highlight the defect location in the entire scan area. In particular, two novel processing techniques are proposed in this paper: a standing wave filter and a Laplacian image filter. Both were found to be effective at detecting delamination, while the latter was also found to be capable of detecting disbonds. By applying both the processing techniques to a scanned image, one can differentiate between a delamination and a disbond. Furthermore, a statistical spatial image processing technique was proposed to identify and locate the defects automatically from the scan images without

needing human intervention. There are certain limitations and opportunities for improvement of the spatial damage detection algorithm. Multiple clusters of outliers resulting from multiple damage will confuse the cluster detection algorithm developed in this study. Also, the centroid detection of the cluster needs to be robust to points outside the cluster. These are envisioned as part of future work.

Acknowledgments

This research is supported by the National Research Foundation of Korea (NRF) under the Ministry of Education, Science & Technology (2010-0017456 and 2010-0020423). The first author would also like to acknowledge the support from the US Air Force Summer Faculty Program. The second author acknowledges the support of the National Science Foundation (NSF award number 0700411).

References

- [1] Sohn H *et al* 2003 A Review of Structural Health Monitoring Literature: 1996–2001 *Technical Report LA-13976-MS* Los Alamos National Laboratory
- [2] Boller C, Chang F and Fujino Y 2009 *Encyclopedia of Structural Health Monitoring* 1st edn (New York: Wiley)
- [3] Lamb H 1917 On waves in an elastic plate *Proc. R. Soc. A* **93** 114–28
- [4] Achenbach J 1987 *Wave Propagation in Elastic Solids* (Amsterdam: North Holland)
- [5] Auld B A 1990 *Acoustic Fields and Waves in Solids* 2nd edn vol 2 (Malabar, FL: Krieger)
- [6] Raghavan A and Cesnik C E 2007 Review of guided-wave structural health monitoring *Shock Vib. Dig.* **39** 91–114
- [7] Zhu W, Rose J L, Barshinger J N and Agarwala V S 1998 Ultrasonic guided wave NDT for hidden corrosion detection *Res. Nondestruct. Eval.* **10** 205–25
- [8] Wilcox P D, Lowe M J S and Cawley P 2001 Mode and transducer selection for long range Lamb wave inspection *J. Intell. Mater. Syst. Struct.* **12** 553–65
- [9] Pelts S P, Jiao D and Rose J L 1996 A comb transducer for guided wave generation and mode selection 1996 *IEEE Ultrasonics Symp.*, 1996 *Proc.* pp 857–60
- [10] Alers G A and Burns L R 1987 EMAT designs for special applications *Mater. Eval.* **45** 1184–9
- [11] Platte M 1987 PVDF—ultrasonic transducers *Ferroelectrics* **75** 327
- [12] Betz D C, Thursby G, Culshaw B and Staszewski W J 2003 Acousto-ultrasonic sensing using fiber Bragg gratings *Smart Mater. Struct.* **12** 122–8
- [13] Scruby C B and Drain L E 1990 *Laser Ultrasonics: Techniques and Applications* (London: Taylor and Francis)
- [14] Leong W H, Staszewski W J, Lee B C and Scarpa F 2005 Structural health monitoring using scanning laser vibrometry: III. Lamb waves for fatigue crack detection *Smart Mater. Struct.* **14** 1387–95
- [15] Staszewski W J, Lee B C and Traynor R 2007 Fatigue crack detection in metallic structures with Lamb waves and 3D laser vibrometry *Meas. Sci. Technol.* **18** 727–39
- [16] Ruzzene M 2007 Frequency–wavenumber domain filtering for improved damage visualization *Smart Mater. Struct.* **16** 2116–29
- [17] Yashiro S, Takatsubo J and Toyama N 2007 An NDT technique for composite structures using visualized Lamb-wave propagation *Compos. Sci. Technol.* **67** 3202–8
- [18] Yashiro S, Takatsubo J, Miyauchi H and Toyama N 2008 A novel technique for visualizing ultrasonic waves in general solid media by pulsed laser scan *NDT&E Int.* **41** 137–44
- [19] Lee J R, Takatsubo J and Toyama N 2007 Disbond monitoring at wing stringer tip based on built-in ultrasonic transducers and a pulsed laser *Smart Mater. Struct.* **16** 1025–35
- [20] Yan F, Royer R L and Rose J L 2010 Ultrasonic guided wave imaging techniques in structural health monitoring *J. Intell. Mater. Syst. Struct.* **21** 377–84
- [21] Giurgiutiu V and Bao J 2004 Embedded-ultrasonics structural radar for *in situ* structural health monitoring of thin-wall structures *Struct. Health Monit.* **3** 121–40
- [22] Lanza di Scalea F and Green R E 1999 High-sensitivity laser-based ultrasonic C-scan system for materials inspection *Exp. Mech.* **39** 329–34
- [23] Dutta D, Sohn H and Yang J Y 2010 A non-contact structural health monitoring system through laser based excitation and sensing of ultrasonic guided waves *USNCTAM2010: Proc. 16th US Natl. Congress of Theoretical and Applied Mechanics (Pennsylvania, 2010)* pp 1–2
- [24] Polytec GmbH, Non-contact vibration measurement 01-Feb-2010 online available: <http://www.polytec.com/usa/158.427.asp> (accessed: 04-Feb-2010)
- [25] Swenson E D, Sohn H, Olson S E and Desimio M P 2010 A comparison of 1D and 3D laser vibrometry measurements of Lamb waves *The Monitoring of Structural and Biological Systems (San Diego, CA)* p 765003
- [26] Krohn N, Pfeleiderer K, Stössel R, Solodov I and Busse G 2004 Nonlinear acoustic imaging: fundamentals, methodology, and NDE-applications *Acoustical Imaging* vol 27 ed W Arnold and S Hirsekorn, pp 91–8
- [27] Willemann D P, Castellini P, Revel G M and Tomasini E P 2004 Structural damage assessment in composite material using laser Doppler vibrometry *Proc. SPIE* **5503** 375
- [28] Hayashi T and Kawashima K 2002 Multiple reflections of Lamb waves at a delamination *Ultrasonics* **40** 193–7
- [29] Liu G R and Achenbach J D 1995 Strip element method to analyze wave scattering by cracks in anisotropic laminated plates *J. Appl. Mech.* **62** 607
- [30] Gonzalez R C, Woods R E and Eddins S L 2003 *Digital Image Processing Using MATLAB* Illustrated edn (Englewood Cliffs, NJ: Prentice Hall)
- [31] Pukelsheim F 1994 The three sigma rule *Am. Stat.* **48** 88–91
- [32] Bailey T and Gatrell T 1996 *Interactive Spatial Data Analysis* (Englewood Cliffs, NJ: Prentice Hall)